Available online at www.sciencedirect.com
SCIENCE DIRECT®
Journal of Computational Physics 196 (2004) 393–416
JOURNAL OF COMPUTATIONAL PHYSICS
www.elsevier.com/locate/jcp

A central-constrained transport scheme for ideal magnetohydrodynamics

U. Ziegler

Astrophysikalisches Institut Potsdam, D-14482 Potsdam, Germany

Received 19 February 2003; received in revised form 10 November 2003; accepted 10 November 2003

Abstract

I propose an easy-to-code numerical scheme for the equations of compressible ideal magnetohydrodynamics (MHD) in multiple space dimensions. The presented method employs the central-upwind scheme of Kurganov et al. [SIAM J. Sci. Comput. 160 (2001) 707] in semi-discrete form combined with the constrained transport technique to satisfy the divergence-free condition for the magnetic field up to machine precision on the numerical grid. A variety of test problems in 1D, 2D and 3D show the robustness and efficiency of this 'hybrid ansatz' which renders it an interesting alternative to existing, numerically more intricate, solvers for the MHD equations.

PACS: 02.60; 95.30.Qd

Keywords: Magnetohydrodynamics; Numerics: central schemes

1. Introduction

Upwind differencing schemes have gained great focus in modeling hydrodynamical phenomena as well as in the numerical integration of other hyperbolic systems of conservation laws. The main advantage of the concept of upwinding is that it provides a natural access to a treatment of shocks and other flow discontinuities without requiring artificial viscosity typical for (non-conservative) operator splitting methods [38,45]. Since the seminal first-order scheme of Godunov [15] higher-order methods based on the upwind approach have been invented. One such famous scheme is the (formally second-order) piecewise parabolic method (PPM) advocated by Colella and Woodward [7]. PPM is characterized by a low numerical diffusion in smooth regions of the flow and its capability to permit a steep representation of captured discontinuities. This is achieved by a flux-limited piecewise parabolic reconstruction algorithm. Higher-order generalizations of Godunov-type upwind schemes have been developed by Harten et al. [16] (see also [36,37]),

E-mail address: uziegler@aip.de (U. Ziegler).
URL: http://www.aip.de.

0021-9991/$ - see front matter
doi:10.1016/j.jcp.2003.11.003

involving essentially non-oscillatory (ENO) piecewise polynomial reconstruction techniques or, more recently, weighted essentially non-oscillatory (WENO) interpolation routines [20,27]. The main disadvantage of upwind schemes is that they require full information about the eigenstructure of the underlying equations which is needed to solve the Riemann problem at cell interfaces or for characteristic decomposition. Problems arise in particular when dealing with more complex physical systems involving, for instance, dissipative forces, chemical reactions between different species, relativistic effects or radiation transport. Upwind schemes then encounter severe difficulties due to degeneracies in the eigensystem and may become not only too intricate to code but also less robust.

A different class of numerical schemes for conservation laws which admit a relatively simple formulation and which do not rely on Riemann solvers are central differencing schemes. The most simplest among them is the Lax–Friedrich scheme [30]. Motivated by the need to reduce the overwhelming numerical dissipation in the Lax–Friedrich method higher-order versions of central schemes have been constructed. The first second-order variant is the scheme of Nessyahu–Tadmor [32]. It uses a linear reconstruction profile in space and employs the midpoint quadrature formula to approximate the time integrals of the fluxes. A genuinely 2D version of the 1D Nessyahu–Tadmor scheme has been developed by the authors in [1,19]. Higher-order extensions of the Nessyahu–Tadmor scheme are reported in [2,31]. Higher-order central schemes which apply a WENO-type reconstruction can be found in [25,26]. A special family of central schemes elaborated in a series of papers [21–24] is characterized by using more precise information of the local propagation speeds, thus, lowering the numerical viscosity further. Again, these types of schemes retain its simplicity over upwind schemes of being independent of the eigenstructure of the problem. One special feature of such 'low-viscosity' methods is that they admit a semi-discrete form. The advantage of such semi-discrete formulation is that it more easily allows to construct genuinely unsplit schemes in multiple space dimensions. A fully discrete version is then recovered by discretizing the set of ODEs in time applying any stable ODE solver, e.g. a Runge–Kutta solver.

The author's interest lies in the numerical modeling of astrophysical phenomena described by the equations of magnetohydrodynamics (MHD). In numerical schemes for the MHD equations the crucial issue is to preserve the divergence constraint $\nabla \cdot \mathbf{B} = 0$ for the magnetic field $\mathbf{B}$ to the highest possible accuracy. This is because magnetic monopols generated by the discretized system lead to unphysical effects, e.g. artificial accelerations transverse to the magnetic field lines and wrong field topologies [3,4]. Several strategies have been proposed to deal with that problem. A natural method which automatically maintains solenoidality is the constrained transport (CT) method. The CT idea, described in detail, e.g. by Evans and Hawley [14], is based on a staggered collocation of the magnetic- and electric field components and employs a special discretization of Faraday's law (induction equation) such that the divergence of the curl of the electric field vanishes numerically. An obvious disadvantage of CT is that it cannot be incorporated as an integral part in Godunov-type schemes which require cell-centered data. Balsara and Spicer [5] in their Godunov-type scheme therefore introduce a second set of (now staggered) magnetic field components. The staggered field is updated with CT preserving $\nabla \cdot \mathbf{B} = 0$ and uses an upwind electric field computed from the base scheme, however, with cell-centered magnetic field data. This approach has proven robust. Similar strategies have been investigated by Toth [39] for different second-order accurate Riemann-solver-based schemes and Ryu et al. [35]. Londrillo and Del Zanna [29] have applied the CT philosophy to a third-order ENO-type central scheme for multi-dimensional, non-relativistic MHD and have proposed explicit upwind formulae for the electric field which do not require the definition of cell-centered magnetic field data. An extension of that scheme to the equations of relativistic MHD has been presented just recently by Del Zanna et al. [12].

A completely different way to remove the unphysical part of the magnetic field is to use a projection method as suggested by Brackbill and Barnes [4]. In the projection method the $\nabla \cdot \mathbf{B} = 0$ violating magnetic field is projected onto the space of divergence-free $\mathbf{B}$-fields after each time-step at the expense of requiring the solution of a Poisson equation. Other methods have been proposed based on propagating and damping

away arising errors in $\nabla \cdot \mathbf{B}$. Powell et al. [33] advocated the use of a modified (eight-wave) Roe-type Riemann solver to maintain the divergence-free constraint at least to a level comparable to the truncation error. This approach propagates errors in $\nabla \cdot \mathbf{B}$ with the fluid velocity and introduces source terms proportional to $\nabla \cdot \mathbf{B}$ in the momentum-, energy-, and induction equation. Modifications of this ansatz are discussed in [9,18]. A combined hyperbolic–parabolic divergence cleaning was studied by Dedner et al. [8] using the so-called generalized Lagrange multiplier method.

In this paper I suggest an easy-to-code method for the solution of the equations of ideal MHD which combines a semi-discrete central scheme with the constrained transport recipe to ensure solenoidality of the magnetic field up to machine precision. The MHD solver is second-order accurate in space and time. The algorithms are discussed in Section 3 after the basic equations have been introduced in Section 2. In Section 4, the scheme is validated by means of a variety of test problems in 1D, 2D and 3D. Some concluding remarks are finally given in Section 5.

2. Equations

The basic equations ought to be solved here numerically are the equations of ideal magnetohydrodynamics given in the conservation form

$$\partial_t \varrho + \nabla \cdot (\varrho \mathbf{v}) = 0, \tag{1}$$

$$\partial_t (\varrho \mathbf{v}) + \nabla \cdot \left[\varrho \mathbf{v}\mathbf{v} + \left(p + \frac{1}{2\mu} |\mathbf{B}|^2 \right) I - \frac{1}{\mu} \mathbf{B}\mathbf{B} \right] = 0, \tag{2}$$

$$\partial_t e + \nabla \cdot \left[\left(e + p + \frac{1}{2\mu} |\mathbf{B}|^2 \right) \mathbf{v} - \frac{1}{\mu} (\mathbf{v} \cdot \mathbf{B}) \mathbf{B} \right] = 0, \tag{3}$$

$$\partial_t \mathbf{B} + \nabla \times \mathbf{E} = 0, \tag{4}$$

subject to the constraint

$$\nabla \cdot \mathbf{B} = 0.$$

Beside the magnetic field $\mathbf{B}$, ϱ is the mass density, e is the (total) energy density, $\mathbf{v}$ is the velocity, $\mathbf{E} = -\mathbf{v} \times \mathbf{B}$ is the electric field and μ is the magnetic permeability. It is assumed that the thermal pressure p can be computed from an ideal gas equation of state

$$p = (\gamma - 1) \left(e - \frac{1}{2} \varrho |\mathbf{v}|^2 - \frac{1}{2\mu} |\mathbf{B}|^2 \right), \tag{5}$$

where γ is the ratio of specific heats.

3. The MHD solver

Eqs. (1)–(4) are approximated on a uniform 3D Cartesian grid indexed $[ijk]$ where (x_i, y_j, z_k) locates the center of the numerical cell spanning a volume $[x_{i-1/2}, x_{i+1/2}] \times [y_{j-1/2}, y_{j+1/2}] \times [z_{k-1/2}, z_{k+1/2}]$. I focus on Cartesian systems here to simplify the presentation. The more general case of orthogonal curvilinear coordinates should cause no principle difficulties and is studied after a covariant version of the scheme is

available. The grid spacings in the x-, y- and z-direction are denoted by δx, δy and δz, respectively. Let $\mathbf{u} = (\varrho, e, m_x = \varrho v_x, m_y = \varrho v_y, m_z = \varrho v_z)$ represent the vector of conserved hydrodynamical variables and let $\overline{\mathbf{u}}_{ijk}$ denote the numerical approximation to the corresponding volume-averaged variables in cell $[ijk]$.

Due to the structure of Faraday's law (Eq. (4)) containing the curl operator instead of the divergence operator, a natural grid representation of the magnetic field vector turns out a staggered collocation of its components to be interpreted then as approximations to the face-averaged field. For the B_x-component, for instance,

$$\overline{B}_{xi-\frac{1}{2},j,k} \approx \frac{1}{\delta y \delta z} \int_{[y_{j-\frac{1}{2}}, y_{j+\frac{1}{2}}] \times [z_{k-\frac{1}{2}}, z_{k+\frac{1}{2}}]} B_x(x_{i-\frac{1}{2}}, y, z) \mathrm{d}y \, \mathrm{d}z.$$

Analogue expressions can be written down for $\overline{B}_{yi,j-\frac{1}{2},k}$ and $\overline{B}_{zi,j,k-\frac{1}{2}}$. The collocation of variables is illustrated in Fig. 1(left).

The numerical scheme proposed in this paper to solve the MHD system profits from two major developments in the field: (i) the semi-discrete central scheme for conservation laws constructed by Kurganov et al. [24] referred to as KNP scheme in the following and (ii) the constrained transport technique to approximate Faraday's law. In essence, the full system, Eqs. (1)–(4), is considered as two subsystems. The first, consisting of Eqs. (1)–(3), represents a system of conservation laws solved with the KNP scheme. Not to review all the details here the KNP scheme as a central scheme does not need (linearized) Riemann solvers and does not suffer from computationally expensive characteristic decomposition. Yet, the scheme has an upwind nature since it incorporates information about the local speeds of wave propagation. The second subsystem, the induction equation (4), is treated with the CT ansatz. However, CT is linked to KNP by utilizing the KNP flux in order to find a proper upwind electric field for use in the CT algorithm.

3.1. Semi-discrete central scheme

To solve Eqs. (1)–(3) the KNP scheme is adapted to MHD where the flux function includes the Lorentz force term. In the original work of [24] the KNP scheme has been derived for 2D systems with third-order accuracy in both a fully discrete version and a semi-discrete variant. A 3D generalization of the fully discrete scheme would be a rather messy task. Generalizing the corresponding semi-discrete scheme to three space dimensions, on the other hand, is straightforward. In unsplit form it reads

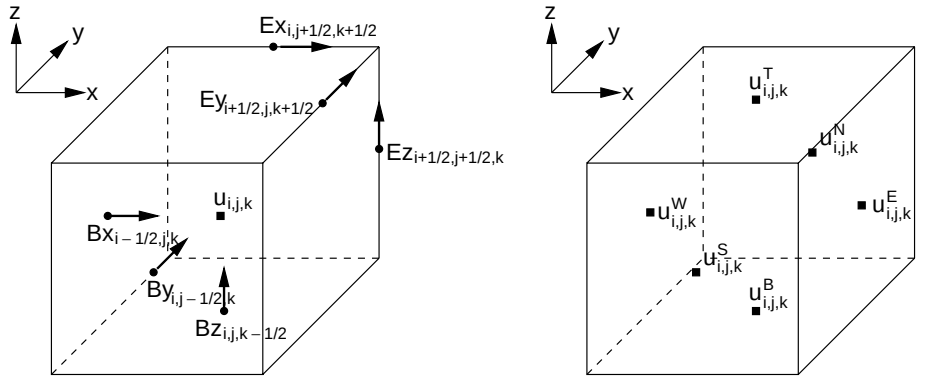

Fig. 1. Left: Collocation of the MHD variables in a 3D cell $[ijk]$. Right: Locations of the reconstructed variables $u^{\mathrm{N(S,W,E,T,B)}}$ (and $B^{\mathrm{N(S,W,E,T,B)}}$ defined at the same locations) appearing in the numerical flux of the KNP scheme.

$$\frac{\mathrm{d}}{\mathrm{d}t}\overline{\mathbf{u}}_{i,j,k}(t) = -\frac{\mathbf{F}^x_{i+\frac{1}{2},j,k}(t) - \mathbf{F}^x_{i-\frac{1}{2},j,k}(t)}{\delta x} - \frac{\mathbf{F}^y_{i,j+\frac{1}{2},k}(t) - \mathbf{F}^y_{i,j-\frac{1}{2},k}(t)}{\delta y} - \frac{\mathbf{F}^z_{i,j,k+\frac{1}{2}}(t) - \mathbf{F}^z_{i,j,k-\frac{1}{2}}(t)}{\delta z}, \tag{6}$$

where

$$\mathbf{F}^x_{i+\frac{1}{2},j,k} = \frac{a^+_{i+\frac{1}{2},j,k}\mathbf{f}^x(\mathbf{u}^{\mathrm{E}}_{i,j,k}, \mathbf{B}^{\mathrm{E}}_{i,j,k}) - a^-_{i+\frac{1}{2},j,k}\mathbf{f}^x(\mathbf{u}^{\mathrm{W}}_{i+1,j,k}, \mathbf{B}^{\mathrm{W}}_{i+1,j,k})}{a^+_{i+\frac{1}{2},j,k} - a^-_{i+\frac{1}{2},j,k}} + \frac{a^+_{i+\frac{1}{2},j,k}a^-_{i+\frac{1}{2},j,k}\left(\mathbf{u}^{\mathrm{W}}_{i+1,j,k} - \mathbf{u}^{\mathrm{E}}_{i,j,k}\right)}{a^+_{i+\frac{1}{2},j,k} - a^-_{i+\frac{1}{2},j,k}},$$

$$\mathbf{F}^y_{i,j+\frac{1}{2},k} = \frac{b^+_{i,j+\frac{1}{2},k}\mathbf{f}^y(\mathbf{u}^{N}_{i,j,k}, \mathbf{B}^{N}_{i,j,k}) - b^-_{i,j+\frac{1}{2},k}\mathbf{f}^y(\mathbf{u}^{S}_{i,j+1,k}, \mathbf{B}^{S}_{i,j+1,k})}{b^+_{i,j+\frac{1}{2},k} - b^-_{i,j+\frac{1}{2},k}} + \frac{b^+_{i,j+\frac{1}{2},k}b^-_{i,j+\frac{1}{2},k}\left(\mathbf{u}^{S}_{i,j+1,k} - \mathbf{u}^{N}_{i,j,k}\right)}{b^+_{i,j+\frac{1}{2},k} - b^-_{i,j+\frac{1}{2},k}},$$

$$\mathbf{F}^z_{i,j,k+\frac{1}{2}} = \frac{c^+_{i,j,k+\frac{1}{2}}\mathbf{f}^z(\mathbf{u}^{T}_{i,j,k}, \mathbf{B}^{T}_{i,j,k}) - c^-_{i,j,k+\frac{1}{2}}\mathbf{f}^z(\mathbf{u}^{B}_{i,j,k+1}, \mathbf{B}^{B}_{i,j,k+1})}{c^+_{i,j,k+\frac{1}{2}} - c^-_{i,j,k+\frac{1}{2}}} + \frac{c^+_{i,j,k+\frac{1}{2}}c^-_{i,j,k+\frac{1}{2}}\left(\mathbf{u}^{B}_{i,j,k+1} - \mathbf{u}^{T}_{i,j,k}\right)}{c^+_{i,j,k+\frac{1}{2}} - c^-_{i,j,k+\frac{1}{2}}},$$

are the numerical fluxes which, of course, depend on time. From Eqs. (1)–(3) the flux functions $\mathbf{f}^x$, $\mathbf{f}^y$ and $\mathbf{f}^z$ are given by

$$\mathbf{f}^x = \begin{pmatrix} m_x \\ \left[(e + p + \mathbf{B}^2/2\mu)m_x - B_x(\mathbf{m}\cdot\mathbf{B})/\mu\right]/\varrho \\ m_x^2/\varrho + p + (-B_x^2 + B_y^2 + B_z^2)/2\mu \\ m_x m_y/\varrho - B_x B_y/\mu \\ m_x m_z/\varrho - B_x B_z/\mu \end{pmatrix},$$

$$\mathbf{f}^y = \begin{pmatrix} m_y \\ \left[(e + p + \mathbf{B}^2/2\mu)m_y - B_y(\mathbf{m}\cdot\mathbf{B})/\mu\right]/\varrho \\ m_x m_y/\varrho - B_x B_y/\mu \\ m_y^2/\varrho + p + (B_x^2 - B_y^2 + B_z^2)/2\mu \\ m_y m_z/\varrho - B_y B_z/\mu \end{pmatrix},$$

$$\mathbf{f}^z = \begin{pmatrix} m_z \\ \left[(e + p + \mathbf{B}^2/2\mu)m_z - B_z(\mathbf{m}\cdot\mathbf{B})/\mu\right]/\varrho \\ m_x m_z/\varrho - B_x B_z/\mu \\ m_y m_z/\varrho - B_y B_z/\mu \\ m_z^2/\varrho + p + (B_x^2 + B_y^2 - B_z^2)/2\mu \end{pmatrix}.$$

The quantities $\mathbf{u}^{\mathrm{N(S,W,E,T,B)}} = (\varrho, e, m_x, m_y, m_z)^{\mathrm{N(S,W,E,T,B)}}$ and $\mathbf{B}^{\mathrm{N(S,W,E,T,B)}} = (B_x, B_y, B_z)^{N(S,E,W,T,B)}$ represent the reconstructed variables at the six face-centered locations $\mathrm{N, S, W, E, T, B}$ (see Fig. 1, right) at time t. $a^\pm$ denotes the maximum (plus sign) and minimum (minus sign) local speed at the cell surface in x-direction, i.e.

$$a^+_{i+\frac{1}{2},j,k} = \max\{(v_x + c_{\mathrm{f}})^{\mathrm{W}}_{i+1,j,k}, (v_x + c_{\mathrm{f}})^{\mathrm{E}}_{i,j,k}, 0\},$$

$$a^-_{i+\frac{1}{2},j,k} = \min\{(v_x - c_{\mathrm{f}})^{\mathrm{W}}_{i+1,j,k}, (v_x - c_{\mathrm{f}})^{\mathrm{E}}_{i,j,k}, 0\},$$

where c_{f} is the fast magnetosonic speed given by

$$c_{\mathrm{f}} = \frac{1}{2}\left[c_{\mathrm{S}}^2 + c_{\mathrm{A}}^2 + \left((c_{\mathrm{S}}^2 + c_{\mathrm{A}}^2)^2 - 4c_{\mathrm{S}}^2\frac{B_x^2}{\mu\varrho}\right)^{1/2}\right]^{1/2}.$$

$c_{\mathrm{S}} = (\gamma p/\varrho)^{1/2}$ is the sound speed and $c_{\mathrm{A}} = (\mathbf{B}^2/\mu\varrho)^{1/2}$ is the Alfvén speed. $b^{\pm}$ ($c^{\pm}$) are the corresponding local speeds in the $y(z)$-direction which one obtains by replacing v_x with $v_y(v_z)$ in the above expressions for $A^{\pm}$ evaluated now at N,S (T,B) positions. Note that the KNP flux is equivalent to the HLL flux formula introduced by Harten, Lax, van Leer as two-speed approximate Riemann solver.

3.2. Reconstruction

Evaluation of the numerical fluxes requires point values of the variables at the centers of the cell surfaces, i.e. at positions E $(x_{i+\frac{1}{2}}, y_j, z_k)$, W $(x_{i-\frac{1}{2}}, y_j, z_k)$, N $(x_i, y_{j+\frac{1}{2}}, z_k)$, S $(x_i, y_{j-\frac{1}{2}}, z_k)$, T $(x_i, y_j, z_{k+\frac{1}{2}})$ and B $(x_i, y_j, z_{k-\frac{1}{2}})$. A linear reconstruction process is used adopting the TVD slope limiter of van Leer [41]. For any hydrodynamical variable at E,W-location, for example,

$$u_{i,j,k}^{\mathrm{E,W}} = \overline{u}_{i,j,k} \pm (\delta_x \overline{u})_{i,j,k},$$

where the plus sign corresponds to the E-location, the minus sign to the W-location and

$$(\delta_x \overline{u})_{i,j,k} = \frac{\max\left\{(\overline{u}_{i+1,j,k} - \overline{u}_{i,j,k})\cdot(\overline{u}_{i,j,k} - \overline{u}_{i-1,j,k}), 0\right\}}{\overline{u}_{i+1,j,k} - \overline{u}_{i-1,j,k}}.$$

Analogue expressions can be derived for the other locations N,S,T,B.

The reconstruction of the magnetic field is as follows. Let us again refer to the E,W-location along the x-direction. Note first that, because of the staggered definition of field components, no reconstruction is needed for B_x in this case. Indeed, that component is already in correct position. For the transverse components B_y and B_z reconstructions are performed to the cell edges and then averaged to the cell surfaces. Thus, at E-location

$$B_{xi,j,k}^{\mathrm{E}} = \overline{B}_{xi+\frac{1}{2},j,k},$$

$$B_{yi,j,k}^{\mathrm{E}} = \frac{1}{2}\left(\overline{B}_{yi,j+\frac{1}{2},k} + \overline{B}_{yi,j-\frac{1}{2},k} + (\delta_x \overline{B}_y)_{i,j+\frac{1}{2},k} + (\delta_x \overline{B}_y)_{i,j-\frac{1}{2},k}\right),$$

$$B_{zi,j,k}^{\mathrm{E}} = \frac{1}{2}\left(\overline{B}_{zi,j,k+\frac{1}{2}} + \overline{B}_{yi,j,k-\frac{1}{2}} + (\delta_x \overline{B}_z)_{i,j,k+\frac{1}{2}} + (\delta_x \overline{B}_z)_{i,j,k-\frac{1}{2}}\right),$$

and at W-location

$$B_{xi,j,k}^{\mathrm{W}} = \overline{B}_{xi-\frac{1}{2},j,k},$$

$$B_{yi,j,k}^{\mathrm{W}} = \frac{1}{2}\left(\overline{B}_{yi,j+\frac{1}{2},k} + \overline{B}_{yi,j-\frac{1}{2},k} - (\delta_x \overline{B}_y)_{i,j+\frac{1}{2},k} - (\delta_x \overline{B}_y)_{i,j-\frac{1}{2},k}\right),$$

$$B_{zi,j,k}^{\mathrm{W}} = \frac{1}{2}\left(\overline{B}_{zi,j,k+\frac{1}{2}} + \overline{B}_{yi,j,k-\frac{1}{2}} - (\delta_x \overline{B}_z)_{i,j,k+\frac{1}{2}} - (\delta_x \overline{B}_z)_{i,j,k-\frac{1}{2}}\right).$$

I omit the corresponding formulae for the N,S,B,T-locations. It should be clear from the context how these look like.

3.3. Constrained transport

From an application of Stoke's theorem a finite-volume discretization of the induction equation (4) is given by

$$\frac{\mathrm{d}}{\mathrm{d}t}\overline{B}_{xi-\frac{1}{2},j,k} = -\frac{\overline{E}_{zi-\frac{1}{2},j+\frac{1}{2},k}(t) - \overline{E}_{zi-\frac{1}{2},j-\frac{1}{2},k}(t)}{\delta y} + \frac{\overline{E}_{yi-\frac{1}{2},j,k+\frac{1}{2}}(t) - \overline{E}_{yi-\frac{1}{2},j,k-\frac{1}{2}}(t)}{\delta z}, \tag{7}$$

$$\frac{\mathrm{d}}{\mathrm{d}t}\overline{B}_{yi,j-\frac{1}{2},k} = \frac{\overline{E}_{zi+\frac{1}{2},j-\frac{1}{2},k}(t) - \overline{E}_{zi-\frac{1}{2},j-\frac{1}{2},k}(t)}{\delta x} - \frac{\overline{E}_{xi,j-\frac{1}{2},k+\frac{1}{2}}(t) - \overline{E}_{xi,j-\frac{1}{2},k-\frac{1}{2}}(t)}{\delta z}, \tag{8}$$

$$\frac{\mathrm{d}}{\mathrm{d}t}\overline{B}_{zi,j,k-\frac{1}{2}} = -\frac{\overline{E}_{yi+\frac{1}{2},j,k-\frac{1}{2}}(t) - \overline{E}_{yi-\frac{1}{2},j,k-\frac{1}{2}}(t)}{\delta x} + \frac{\overline{E}_{xi,j+\frac{1}{2},k-\frac{1}{2}}(t) - \overline{E}_{xi,j-\frac{1}{2},k-\frac{1}{2}}(t)}{\delta y}, \tag{9}$$

where

$$\overline{E}_{xi,j-\frac{1}{2},k-\frac{1}{2}} \approx \frac{1}{\delta x}\int_{[x_{i-\frac{1}{2}},x_{i+\frac{1}{2}}]} E_x(x, y_{j-\frac{1}{2}}, z_{k-\frac{1}{2}})\mathrm{d}x,$$

$$\overline{E}_{yi-\frac{1}{2},j,k-\frac{1}{2}} \approx \frac{1}{\delta y}\int_{[y_{j-\frac{1}{2}},y_{j+\frac{1}{2}}]} E_y(x_{i-\frac{1}{2}}, y, z_{k-\frac{1}{2}})\mathrm{d}y,$$

$$\overline{E}_{zi-\frac{1}{2},j-\frac{1}{2},k} \approx \frac{1}{\delta z}\int_{[z_{k-\frac{1}{2}},z_{k+\frac{1}{2}}]} E_z(x_{i-\frac{1}{2}}, y_{j-\frac{1}{2}}, z)\mathrm{d}z,$$

are approximations to the line-averaged electric field components defined at cell edges as shown in Fig. 1(left). Recall the definition of the $\overline{B}$'s as numerical approximations to the face-averaged magnetic field components. Like the hydro fluxes the electric field components at this stage are time-dependent quantities since no time discretization is given yet. The time rate of change of discretized divergence in cell $[ijk]$ evaluated using $\overline{\mathbf{B}}$-data becomes to second-order

$$\frac{\mathrm{d}}{\mathrm{d}t}(\nabla\cdot\overline{\mathbf{B}})_{i,j,k} = \frac{\frac{\mathrm{d}}{\mathrm{d}t}\overline{B}_{xi+\frac{1}{2},j,k} - \frac{\mathrm{d}}{\mathrm{d}t}\overline{B}_{xi-\frac{1}{2},j,k}}{\delta x} + \frac{\frac{\mathrm{d}}{\mathrm{d}t}\overline{B}_{yi,j+\frac{1}{2},k} - \frac{\mathrm{d}}{\mathrm{d}t}\overline{B}_{yi,j-\frac{1}{2},k}}{\delta y} + \frac{\frac{\mathrm{d}}{\mathrm{d}t}\overline{B}_{zi,j,k+\frac{1}{2}} - \frac{\mathrm{d}}{\mathrm{d}t}\overline{B}_{zi,j,k-\frac{1}{2}}}{\delta z}.$$

Using Eqs. (7)–(9) one easily derives $\mathrm{d}(\nabla\cdot\overline{\mathbf{B}})_{i,j,k}/\mathrm{d}t = 0$ since electric field components pairwise cancel. Hence, if $\nabla\cdot\overline{\mathbf{B}} = 0$ everywhere initially, the evolved magnetic field remains solenoidal.

The electric field in Eqs. (7)–(9) takes on the role of the fluxes in Eq. (6) and the main question is how to compute it properly. The recipe applied here is rather simple and relies on utilizing the KNP scheme:

(i) Note first that the induction equation can be transformed into divergence form with an antisymmetric flux tensor, i.e.

$$\partial_t\mathbf{B} = -\nabla\times\mathbf{E} = \nabla\cdot\begin{pmatrix} 0 & E_z & -E_y \\ -E_z & 0 & E_x \\ E_y & -E_x & 0 \end{pmatrix}.$$

(ii) From the flux tensor construct numerical fluxes $\mathbf{E}^x, \mathbf{E}^y, \mathbf{E}^z$ using the KNP flux formula. These fluxes are definitely defined at cell surfaces like their hydrodynamical counterparts $\mathbf{F}^x, \mathbf{F}^y, \mathbf{F}^z$. The resulting expressions read:

$$\mathbf{E}^x_{i+\frac{1}{2},j,k} = \frac{1}{a^+_{i+\frac{1}{2},j,k} - a^-_{i+\frac{1}{2},j,k}} \left[a^+_{i+\frac{1}{2},j,k} \begin{pmatrix} 0 \\ -E_z \\ E_y \end{pmatrix}^{\mathrm{E}}_{i,j,k} - a^-_{i+\frac{1}{2},j,k} \begin{pmatrix} 0 \\ -E_z \\ E_y \end{pmatrix}^{\mathrm{W}}_{i+1,j,k} + a^+_{i+\frac{1}{2},j,k} a^-_{i+\frac{1}{2},j,k} \left(\mathbf{B}^{\mathrm{W}}_{i+1,j,k} - \mathbf{B}^{\mathrm{E}}_{i,j,k} \right) \right],$$

$$\mathbf{E}^y_{i,j+\frac{1}{2},k} = \frac{1}{b^+_{i,j+\frac{1}{2},k} - b^-_{i,j+\frac{1}{2},k}} \left[b^+_{i,j+\frac{1}{2},k} \begin{pmatrix} E_z \\ 0 \\ -E_x \end{pmatrix}^{N}_{i,j,k} - b^-_{i,j+\frac{1}{2},k} \begin{pmatrix} E_z \\ 0 \\ -E_x \end{pmatrix}^{S}_{i,j+1,k} + b^+_{i,j+\frac{1}{2},k} b^-_{i,j+\frac{1}{2},k} \left(\mathbf{B}^{S}_{i,j+1,k} - \mathbf{B}^{N}_{i,j,k} \right) \right],$$

$$\mathbf{E}^z_{i,j,k+\frac{1}{2}} = \frac{1}{c^+_{i,j,k+\frac{1}{2}} - c^-_{i,j,k+\frac{1}{2}}} \left[c^+_{i,j,k+\frac{1}{2}} \begin{pmatrix} -E_y \\ E_x \\ 0 \end{pmatrix}^{T}_{i,j,k} - c^-_{i,j,k+\frac{1}{2}} \begin{pmatrix} -E_y \\ E_x \\ 0 \end{pmatrix}^{B}_{i,j,k+1} + c^+_{i,j,k+\frac{1}{2}} c^-_{i,j,k+\frac{1}{2}} \left(\mathbf{B}^{B}_{i,j,k+1} - \mathbf{B}^{T}_{i,j,k} \right) \right],$$

where $\mathbf{E}^{\mathrm{N(S,W,E,T,B)}} = -\mathbf{v}^{\mathrm{N(S,W,E,T,B)}} \times \mathbf{B}^{\mathrm{N(S,W,E,T,B)}}$ denotes the reconstructed electric field vector at N(S,W,E,T,B)-location.

(iii) From the face-centered fluxes obtained in that way compute edge-centered electric fields by suitable interpolations, i.e.

$$\overline{E}_{xi,j-\frac{1}{2},k-\frac{1}{2}} = \frac{1}{4}(-E^y_{zi,j-\frac{1}{2},k} - E^y_{zi,j-\frac{1}{2},k-1} + E^z_{yi,j,k-\frac{1}{2}} + E^z_{yi,j-1,k-\frac{1}{2}}),$$

$$\overline{E}_{yi-\frac{1}{2},j,k-\frac{1}{2}} = \frac{1}{4}(E^x_{zi-\frac{1}{2},j,k} + E^x_{zi-\frac{1}{2},j,k-1} - E^z_{xi,j,k-\frac{1}{2}} - E^z_{xi-1,j,k-\frac{1}{2}}),$$

$$\overline{E}_{zi-\frac{1}{2},j-\frac{1}{2},k} = \frac{1}{4}(-E^x_{yi-\frac{1}{2},j,k} - E^x_{yi-\frac{1}{2},j-1,k} + E^y_{xi,j-\frac{1}{2},k} + E^y_{xi-1,j-\frac{1}{2},k}),$$

for use in the updating formulae (7)–(9).

Remark.

- The above composition rules are for the 3D case. In 2D on a $[ij]$-grid

$$\overline{E}_{xi,j-\frac{1}{2}} = -E^y_{zi,j-\frac{1}{2}},$$

$$\overline{E}_{yi-\frac{1}{2},j} = E^x_{zi-\frac{1}{2},j},$$

$$\overline{E}_{zi-\frac{1}{2},j-\frac{1}{2}} = \frac{1}{4}(-E^x_{yi-\frac{1}{2},j} - E^x_{yi-\frac{1}{2},j-1} + E^y_{xi,j-\frac{1}{2}} + E^y_{xi-1,j-\frac{1}{2}}),$$

and in 1D on a $[i]$-grid

$$\overline{E}_{xi} = 0,$$

$$\overline{E}_{yi-\frac{1}{2}} = E^x_{zi-\frac{1}{2}},$$

$$\overline{E}_{zi-\frac{1}{2}} = -E^x_{yi-\frac{1}{2}}.$$

- The idea to calculate the electric field fluxes for the CT update from the underlying conservative base scheme (here the KNP scheme) follows closely the work of [5,35,39]. Balsara and Spicer [5] introduced a staggered **B** which is updated with CT coexisting with a cell-centered **B** used to compute fluxes in their upwind scheme. However, as pointed out by these authors, it may sometimes become necessary to recompute the pressure using the staggered magnetic field violating energy conservation, i.e. consistency of the induction equation with the energy equation is lost. This is not the case here since no cell-centered field is involved and all the reconstruction is based on the staggered magnetic field components.
- The various interpolation procedures likely introduce some additional amount of diffusion but do not destroy the second-order accuracy of the full MHD scheme on smooth flows which is experimentally proved below (Section 4.2). Furthermore, interpolation enlarges the stencil which complicates parallelization tasks and the carry-over of the scheme to adaptive grids.
- An interesting alternative to calculate electric field fluxes for the induction equation which does not rely on face-to-edge interpolation has been discussed by Zanna et al. [12] in their ENO-type central scheme. They propose a HLL formula for **E** which is a modification of the corresponding formula for the hydro flux taking into account the staggered collocation of **B**. This formula is based on four-state quantities (instead of two in the hydro fluxes) for each **E**-component. Although no rigorous derivation has been given by [12], their formulation is strongly motivated by the fact that it matches exactly the HLL formula described in [24] for Hamilton–Jacobi equations to what the induction equation in 2D reduces for given velocity field.

3.4. Time integration

The full system of ODEs is integrated with a second-order Runge–Kutta scheme. Denoting the right-hand side of Eq. (6) as $F[\overline{\mathbf{u}}, \overline{\mathbf{B}}]$ and the right-hand sides of Eqs. (7)–(9) as $E[\overline{\mathbf{u}}, \overline{\mathbf{B}}]$ then

$$\overline{\mathbf{u}}^{*} = \overline{\mathbf{u}}^{n} + \delta t \cdot F[\overline{\mathbf{u}}^{n}, \overline{\mathbf{B}}^{n}],$$

$$\overline{\mathbf{B}}^{*} = \overline{\mathbf{B}}^{n} + \delta t \cdot E[\overline{\mathbf{u}}^{n}, \overline{\mathbf{B}}^{n}],$$

$$\overline{\mathbf{u}}^{n+1} = \frac{1}{2}\overline{\mathbf{u}}^{n} + \frac{1}{2}(\overline{\mathbf{u}}^{*} + \delta t \cdot F[\overline{\mathbf{u}}^{*}, \overline{\mathbf{B}}^{*}]),$$

$$\overline{\mathbf{B}}^{n+1} = \frac{1}{2}\overline{\mathbf{B}}^{n} + \frac{1}{2}(\overline{\mathbf{B}}^{*} + \delta t \cdot E[\overline{\mathbf{u}}^{*}, \overline{\mathbf{B}}^{*}]),$$

where δt is the numerical time-step restricted by the usual CFL criterion.

4. MHD test problems

The new scheme, which is referred to as KNPCT in the following, has been implemented in the NIRVANA code developed by the author (see [45,46]) and already used in many different astrophysical simulations (e.g. [43,44,47]). KNPCT is validated in one-, two- and three space dimensions. For the most test problems presented here reference solutions exist in the literature obtained with different codes. Beside a comparison with literature results, it is instructive to compare KNPCT with the previous NIRVANA solver

(called FD in the following) – a non-conservative, operator-splitting scheme which makes use of tensor artificial viscosity due to Tscharnuter and Winkler [40] to treat shocks. If not otherwise stated, in all test problems the magnetic permeability $\mu = 1$ and the artificial viscosity coefficient $q = 1.5$ in the FD scheme.

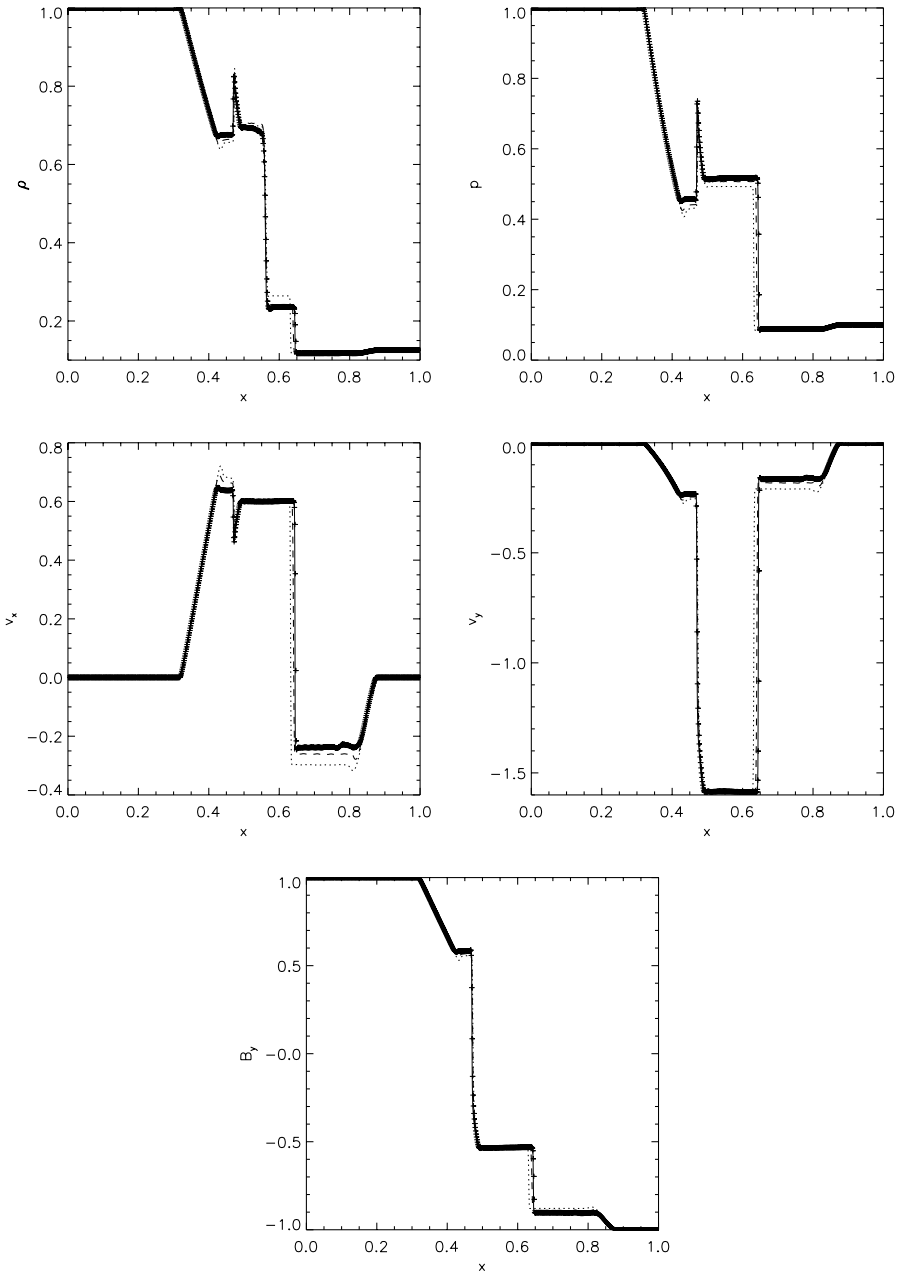

Fig. 2. Numerical solution of the Brio–Wu Riemann problem for the KNPCT solver (plus signs), FD solver with $q = 1.5$ (dotted lines) and FD solver with $q = 4$ (dashed lines) for $N = 800$. The primitive variables ϱ, p, v_x, v_y and B_y are shown. The solid curve in each plot represents the reference solution.

A quantitative comparison of results is done by computing errors relative to the analytic solution, if available, or a high-resolution run which then serves as reference solution. The relative error of some variable u is denoted E_u and is expressed in the L_1 norm

$$E_u = \frac{\sum_{ijk} |u_{i,j,k} - u^{\mathrm{ref}}_{i,j,k}|}{\sum_{ijk} |u^{\mathrm{ref}}_{i,j,k}|}$$

(for the 3D cases). The averaged error, $\overline{E}$, is the mean of all or some E_u. From a comparison of errors at different numerical resolutions the convergence rate of the schemes can be determined. This experimental order of convergence (EOC) is obtained for all test problems.

4.1. 1D: Brio–Wu Riemann problem

In the MHD Riemann problem of Brio and Wu [6] one considers initial data consisting of the two constant states

$$\begin{pmatrix} \varrho \\ p \\ v_x \\ v_y \\ v_z \\ B_x \\ B_y \\ B_z \end{pmatrix}^L = \begin{pmatrix} 1 \\ 1 \\ 0 \\ 0 \\ 0 \\ 0.75 \\ 1 \\ 0 \end{pmatrix}, \qquad \begin{pmatrix} \varrho \\ p \\ v_x \\ v_y \\ v_z \\ B_x \\ B_y \\ B_z \end{pmatrix}^R = \begin{pmatrix} 0.125 \\ 0.1 \\ 0 \\ 0 \\ 0 \\ 0.75 \\ -1 \\ 0 \end{pmatrix}.$$

The interface separating the left and right state is located at $x = 0.5$. The computational domain is $x \in [0, 1]$. The initial data are evolved up to time $t = 0.1$ using a value $\gamma = 2$ in the equation of state (5). Calculations for both solvers, the FD solver and KNPCT solver, are performed on different grids with $N = 100, 200, 400, 800$ zones. Since no analytical solution is known for this problem, a high-resolution KNPCT run with $N = 3200$ serves as reference solution. Note that the results are directly comparable with those presented in [6] using a second-order upwind scheme with approximate Riemann solver specifically designed for that problem.

Fig. 2 presents the results of the computations for $N = 800$. The KNPCT solution shows slight oscillations between the shock and right rarefaction wave but otherwise compares favorable with the solution given in [6]. The KNPCT solver obviously converges against the reference solution with an EOC of approximately 1 (see Table 1 whereas the FD scheme fails to do so. The FD solution strongly depends on the amount of artificial viscosity and clearly has wrong states left and right to the shock with the shock itself propagating at a too low speed. The failure of the FD solver is clearly a consequence of its non-conservative

Table 1
Brio–Wu Riemann problem

N	FD				KNPCT		
	$\overline{E}$	$\overline{E}$[a]	EOC	Time (s)	$\overline{E}$	EOC	Time (s)
100	0.0802	0.0470		5	0.0555		2
			0.51			0.87	
200	0.0667	0.0329		22	0.0301		8
			0.31			1.05	
400	0.0598	0.0267		89	0.0144		31
			0.20			1.03	
800	0.0559	0.0233		353	0.0071		123

[a] With stronger artificial viscosity $q = 4$.

character. Table 1 reports the averaged error, $\overline{E}$, defined as the mean of the individual errors of the primitive variables ϱ, p, v_x, v_y and B_y. B_x remains exactly constant, hence, does not contribute to $\overline{E}$.

4.2. 2D: Circularly polarized Alfvén waves

The propagation of a monochromatic circularly polarized Alfvén wave is studied. The purpose of this test problem is to check the second-order accuracy of the KNPCT scheme. The direction of propagation is along the diagonal $x = y$ on the 2D domain $(x, y) = [0, 1]^2$ discretized by a $N \times N$ grid. Periodic boundary conditions are adopted in both coordinate directions. At $t = 0$, the density $\varrho = 1$ and pressure $p = 0.1$. The velocity and magnetic field components parallel respective transverse to the diagonal are

$$v_\parallel = 0, \quad B_\parallel = B_0,$$

$$v_\perp = -B_\perp = A \sin\left(\frac{2\pi}{\lambda}\hat{\mathbf{k}} \cdot \mathbf{x}\right),$$

where $\hat{\mathbf{k}} = \left(1/\sqrt{2}, 1/\sqrt{2}\right)$ is the unit vector in the direction of propagation. From the parallel- and transverse components one can compute the Cartesian components according to

$$\begin{pmatrix} B_x \\ B_y \end{pmatrix} = \begin{pmatrix} \frac{1}{\sqrt{2}} & \frac{1}{\sqrt{2}} \\ \frac{1}{\sqrt{2}} & \frac{1}{\sqrt{2}} \end{pmatrix} \cdot \begin{pmatrix} B_\parallel \\ B_\perp \end{pmatrix}.$$

The z-component of the vector fields are

$$v_z = -B_z = A \cos\left(\frac{2\pi}{\lambda}\hat{\mathbf{k}} \cdot \mathbf{x}\right).$$

The parameters of the problem are chosen to $A = 0.01$, $B_0 = \sqrt{2}$ and $\lambda = 1/\sqrt{2}$. Hence, there are exact two wavelengths in the diagonal and the period of motion is given by $P = \lambda/c_A = 0.5$. The system is evolved one period after which the resulting wave pattern should ideally match the initial profile. I calculate the error E_{v_z} in the vertical velocity for grids $N = 20, 40, 80, 160$. Fig. 3 shows that error as a function of the number of grid points in a double logarithmic scale. As expected, second-order accuracy is achieved.

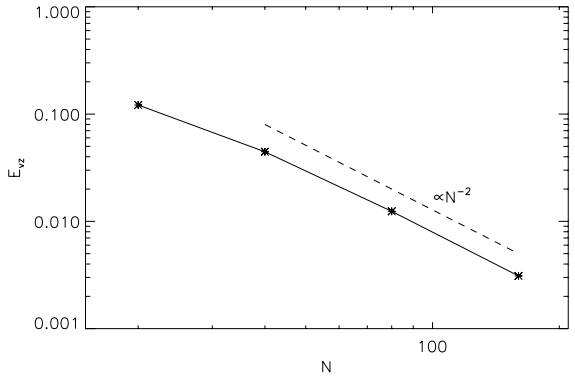

Fig. 3. Order-of-accuracy check of the KNPCT scheme for the Alfvén wave problem. The error in v_z is plotted as a function of the number of grids points indicating second-order convergence.

4.3. 2D: Oblique Riemann problem

This 2D test has been used, for instance, by the authors in [10,34,35,39]. A 1D Riemann problem with initial left and right states

$$\begin{pmatrix} \varrho \\ p \\ v_\parallel \\ v_\perp \\ B_\parallel \\ B_\perp \end{pmatrix}^L = \begin{pmatrix} 1 \\ 20 \\ 10 \\ 0 \\ B_0 \\ B_0 \end{pmatrix}, \qquad \begin{pmatrix} \varrho \\ p \\ v_\parallel \\ v_\perp \\ B_\parallel \\ B_\perp \end{pmatrix}^R = \begin{pmatrix} 1 \\ 1 \\ -10 \\ 0 \\ B_0 \\ B_0 \end{pmatrix}$$

is transformed onto a 2D domain such that the discontinuous interface lies at an angle α to the y-axis in a Cartesian coordinate system (see Fig. 4). The resulting x-respective y-component of the vector fields are derived from their given parallel- and transverse components according to

$$\begin{pmatrix} v_x \\ B_x \end{pmatrix} = \begin{pmatrix} v_\parallel \\ B_\parallel \end{pmatrix} \cos\alpha - \begin{pmatrix} v_\perp \\ B_\perp \end{pmatrix} \sin\alpha,$$

$$\begin{pmatrix} v_y \\ B_y \end{pmatrix} = \begin{pmatrix} v_\parallel \\ B_\parallel \end{pmatrix} \sin\alpha + \begin{pmatrix} v_\perp \\ B_\perp \end{pmatrix} \cos\alpha.$$

The 2D problem is solved on a $N \times 4$ grid spanning a narrow strip $(x, y) = [0, 1] \times [-2/N, 2/N]$. To give that a sense shift-periodic boundary conditions are applied on the upper and lower y-boundary similar to [39]. On the x-boundaries variables are fixed at their initial values since the simulations are stopped before the fastest waves reach these boundaries.

The realization of shift-periodic boundary conditions becomes especially simple for certain α satisfying the condition $4/N \tan\alpha = m\delta x$ or $4\tan\alpha = m$ with m some integral number and $\delta x = \delta y = 1/N$ the grid spacing. I choose $\tan\alpha = 2$ ($\alpha \approx 63^\circ$), i.e. $m = 8$. In discretized form the shift-periodic boundary condition on the upper (lower) y-boundary then reads $u_{i,j_u} = u_{i+8,j_u-4}$ ($u_{i,j_l} = u_{i-8,j_l+4}$) where u is any variable indexed by $[ij]$ with two ghost zones j_u (j_l) on the upper (lower) side. Simulations for different resolutions $N = 128, 256, 512, 1024$ are performed. Results along the line $y = 0$ at time $t = 0.08\cos\alpha$ are compared against a high-resolution ($N = 2048$) 1D ($\alpha = 0$) calculation stopped at $t = 0.08$. This reference solution has been computed with the KNPCT solver.

The solutions generated by both solvers for $N = 256$ are illustrated in Fig. 5. The quantities ϱ, p, $v_\parallel = v_x\cos\alpha + v_y\sin\alpha$, $v_\perp = -v_x\sin\alpha + v_y\cos\alpha$, $B_\parallel = B_x\cos\alpha + B_y\sin\alpha$ and $B_\perp = -B_x\sin\alpha + B_y\cos\alpha$ are shown. The KNPCT (FD) result is represented by plus signs (dashed lines). Solid lines in Fig. 5 depict the reference solution. The averaged error, $\overline{E}$, which is defined here as the mean value of E_ϱ, E_p, $E_{v_\parallel}$, $E_{v_\perp}$, $E_{B_\parallel}$ and $E_{B_\perp}$, respectively, as well as the convergence properties of both schemes are summarized in Table 2. Note

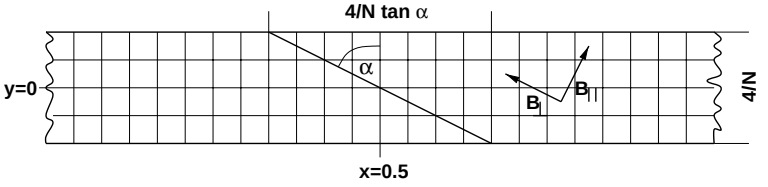

Fig. 4. Illustration of the setup of the oblique Riemann problem.

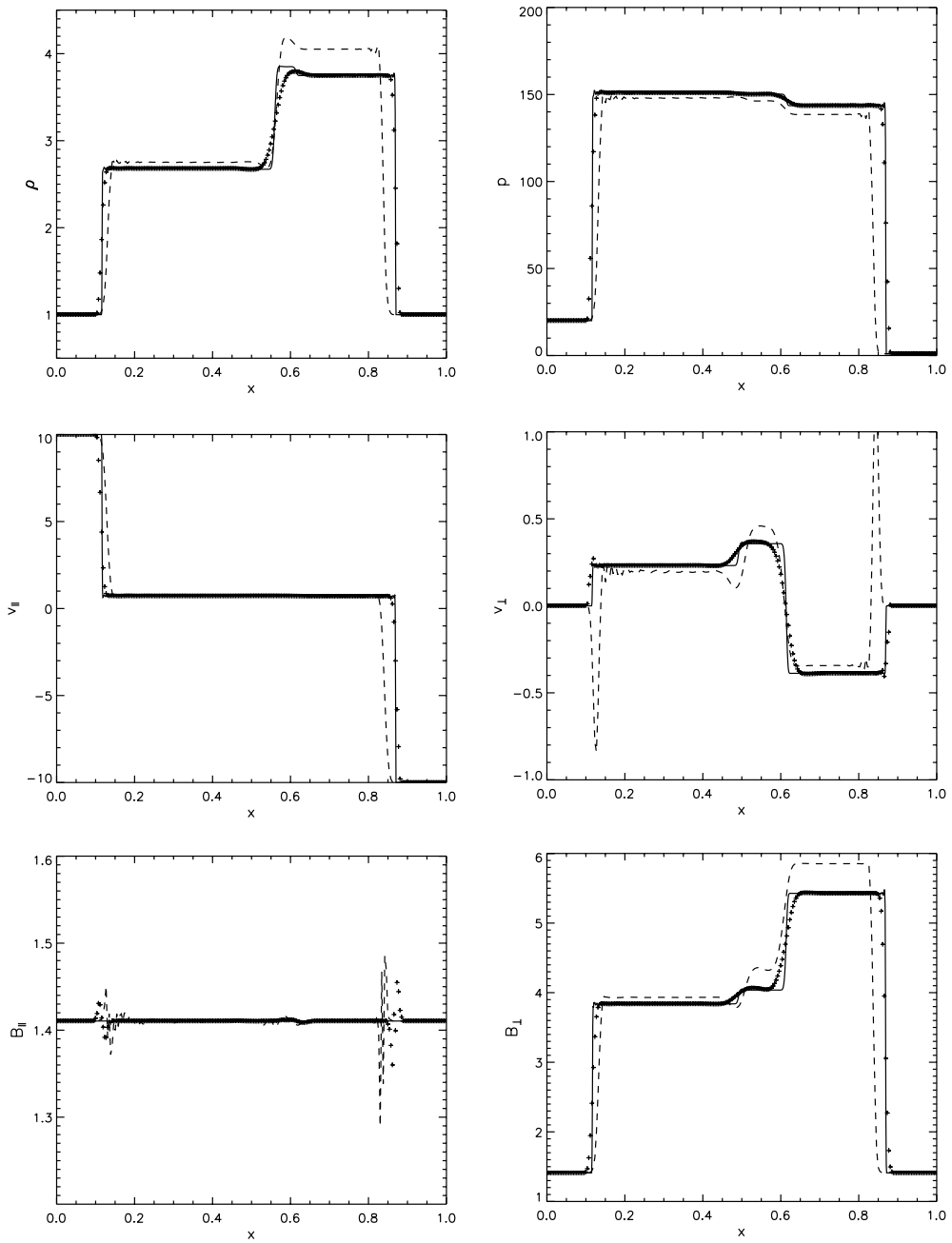

Fig. 5. Numerical solution of the oblique Riemann problem. Results ($N = 256$) are shown for the KNPCT solver (plus signs) and FD solver (dashed lines). The reference solution is given by the solid line.

first that, in spite of the use of artificial viscosity, the FD solver produces a rather bad solution (both the leftgoing and rightgoing fast shocks are not in correct position, large spikes are generated in the variable $v_\perp$, wrong intermediate states are occupied best visible in the ϱ- and $B_\perp$-profiles) and non-convergence against

Table 2
Oblique Riemann problem

N	FD			KNPCT		
	$\overline{E}$	EOC	Time (s)	$\overline{E}$	EOC	Time (s)
128	0.1644		11	0.0430		4
		0.30			0.96	
256	0.1332		44	0.0220		18
		0.15			0.97	
512	0.1199		176	0.0113		71
		0.08			1.03	
1024	0.1136		699	0.0057		301

the reference solution results. In passing I note that without artificial viscosity FD produces a totally wrong solution. The KNPCT scheme converges with EOC ≈ 1. The resulting errors are comparable to those reported in [39] found for different second-order upwind schemes. More specifically, when compared with the corresponding plots in [39], the KNPCT solver performs better on $B_{\|}$ (which ideally should remain unchanged from its initial value) than any scheme tested in [39] but, as might be expected for a central scheme, is slightly less sharp at the contact discontinuities.

4.4. 2D: Orszag–Tang vortex

The Orszag–Tang vortex problem is given by the following initial conditions on a square domain $(x, y) = [0, 2\pi]^2$:

$$\varrho = 25/9, \quad p = 5/3, \quad \mathbf{v} = \begin{pmatrix} -\sin y \\ \sin x \\ 0 \end{pmatrix}, \quad \mathbf{B} = \begin{pmatrix} -\sin y \\ \sin(2x) \\ 0 \end{pmatrix}.$$

Periodic boundary conditions are adopted in both coordinate directions and $\gamma = 5/3$. Numerical results for both types of solvers are calculated on a N^2 grid with $N = 50, 100, 200$ zones. The resulting numerical errors are computed relative to a reference solution obtained with the KNPCT solver using $N = 400$ zones. Note that the initial setup of the problem is identical to that in [39], thus, allowing a direct comparison. Unlike in [39], however, I do not fix the numerical time-step but fix the Courant number $C = 0.4$. Errors are measured at the evolution time $t = 3.14$ when the initially smooth flow has turned into turbulence and has developed a complex structure which contains discontinuities.

The resulting error in the temperature, E_T, and the averaged error, $\overline{E}$, defined here as the mean value of the errors of the primitive variables $\varrho, p, v_x, v_y, B_x, B_y$ is listed in Table 3. The temperature distribution in the half-plane $x < \pi$ and for resolution $N = 200$ is shown in Fig. 6. At first site the FD result and the KNPCT

Table 3
Orszag–Tang vortex

N	FD				KNPCT			
	E_T	$\overline{E}$	EOC	Time (s)	E_T	$\overline{E}$	EOC	Time (s)
50	0.0891	0.1581		14	0.0791	0.1478		17
			0.67				0.87	
100	0.0723	0.0995		116	0.0416	0.0809		135
			0.49				1.34	
200	0.0682	0.0710		1037	0.0170	0.0319		1178
50[a]	0.1336	0.3017		10				
			0.51					
100[a]	0.1209	0.1419		74				
			0.26					
200[a]	0.1171	0.1183		646				

[a] Without artificial viscosity.

result look quit similar. A more detailed inspection of the data, however, offers some discrepancies. For instance, the point of intersection of weak discontinuities located at $(x,y) \approx (2.2, 2.8)$ in the reference solution is located at $(x,y) \approx (2.1, 2.9)$ in the FD solution. FD becomes even worse without artificial viscosity. Somewhat surprisingly, the KNPCT scheme converges at a rate 1.34 which is larger than unity expected for flows dominated by discontinuities. When compared with literature (see e.g. [11,29,39,42]) the KNPCT solver produces as accurate results as its Riemann-solver-based counterparts.

4.5. 2D: Rotor problem

The rotor problem has been suggested by Balsara and Spicer [5] as a test to check the propagation of torsional Alfvén waves. The initial condition consists of a rapidly rotating cylinder of dense gas embedded in a lighter fluid at rest. The system is threaded by a uniform magnetic field along the x-axis and the problem is defined on the 2D Cartesian domain $(x,y) \in [-0.5, 0.5]^2$. With $r = (x^2 + y^2)^{1/2}$ it is

$$\varrho = 1 + 9f(r),$$

$$p = 1,$$

$$v_x = -2f(r)y/r, \quad v_y = 2f(r)x/r, \quad v_z = 0,$$

$$B_x = 5/\sqrt{4\pi}, \quad B_y = B_z = 0,$$

where

$$f(r) = \begin{cases} 1 & \text{if } r < 0.1, \\ \frac{200}{3}(0.115 - r) & \text{if } 0.1 \leqslant r \leqslant 0.115, \\ 0 & \text{if } r > 0.115. \end{cases}$$

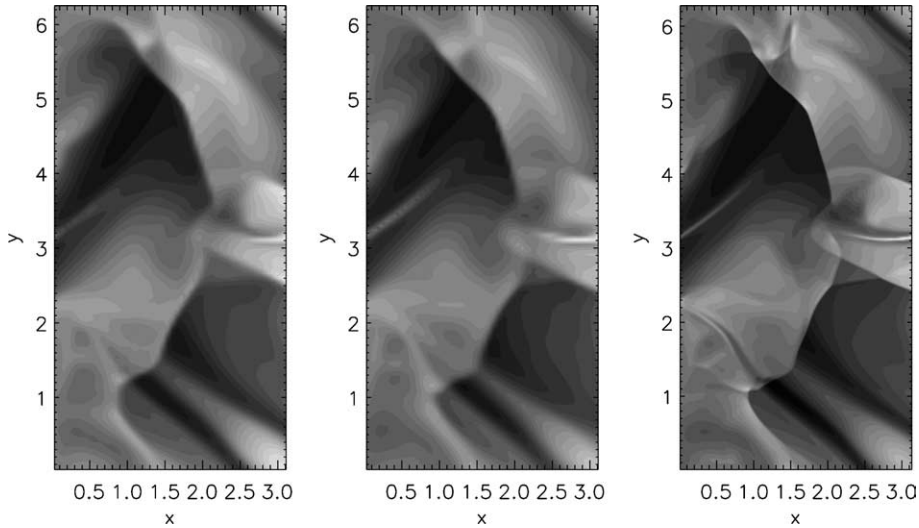

Fig. 6. Gray-scale image of the temperature distribution in the Orszag–Tang vortex problem for the FD solver (left) and KNPCT solver (middle) with $N = 200$ and for the reference solution (right). The range of data is 0.15(black) $< p/\varrho <$ 1.24(white).

The function $f(r)$ serves to smooth the discontinuities in the density and velocity at the cylinder surface by letting both quantities vary in a linear fashion over a small distance $\delta r = 0.015$ from the inner state ($r < 0.1$) to the outer state ($r > 0.115$). The adiabatic index $\gamma = 1.4$. Note that this configuration is identical to that in [39] named there 'first rotor problem'. Runs are carried out on a $N \times N$ grid for $N = 50, 100, 200, 400$ zones. A KNPCT simulation with $N = 800$ serves as reference solution. Zero-gradient boundary conditions (open conditions) are applied in x and y for all variables including the staggered magnetic field components.

In Fig. 7 contour plots of the pressure and Mach number, $|\mathbf{v}|/c_s$ where $c_s = (\gamma p/\varrho)^{1/2}$ is the sound speed, are shown at the final time $t = 0.15$. Since centrifugal forces of the rotor are not compensated at the beginning the denser fluid tends to expand radially. However, the winding up of the magnetic field accompanied by an increase in magnetic pressure stops expansion and the dense gas remains confined. As a consequence of the interplay of forces the geometrical shape becomes elongated in x-direction. This deformation of the inner part is clearly seen in Fig. 7. A complicated structure of torsional Alfvén waves develops which mediate an exchange of angular momentum between the rotating, inner part and the ambient medium.

A quantitative measure of the quality of results in terms of the averaged error of primitive variables is compiled in Table 4. For the lower resolutions studied ($N = 50, 100$) both type of schemes perform roughly similar. For the larger resolutions ($N = 200, 400$), however, the KNPCT solver gives smaller errors and a convergence rate EOC > 1 despite the presence of sharp structures. Note again the bad convergence properties of FD which, moreover, shows slight asymmetries in the solution in particular striking in the Mach number plot showing a distortion of the central, oblate region of rotating fluid. Such asymmetries are not adherent to the KNPCT scheme and the results, in general, compete with those obtained with more sophisticated Riemann-solver-based schemes [5,39].

4.6. 3D: Spherical explosion

A problem of astrophysical interest is the simulation of a spherical explosion involving strong shocks. The problem is set up on a unit cube $(x, y, z) \in [-1/2, 1/2]^3$ spanned by a grid with $N \times N \times N$ zones. The density $\varrho = 1$ everywhere and the initial velocity is zero. The explosion is initiated by a large overpressure in a small spherical region of radius $r = 0.1$:

$$p = \begin{cases} 10^4 & \text{if } x^2 + y^2 + z^2 < r^2, \\ 1 & \text{otherwise.} \end{cases}$$

A uniform magnetic field $B_y = 100$ is applied and $B_x = B_z = 0$. Note that in the surrounding medium the plasma-β ($= 2 \times 10^{-4}$) is rather small. Thermal properties are described by an adiabatic index of $\gamma = 5/3$. Similar problems in two space dimensions can be found in [5,42].

Runs with different resolution $N = 64, 96, 144$ have been performed. Fig. 8 illustrates the solution for $N = 96$ after a time $t = 2.5 \times 10^{-3}$. Contour plots of the magnetic pressure are presented. Due to the presence of the strong magnetic field the explosion becomes highly anisotropic. The spherically symmetric shock characteristic for the field-free situation is split here into two shock fronts propagating parallel to the magnetic field in $\pm y$-direction. Magnetosonic waves are launched traveling in the transverse direction. A detailed look at the magnetic pressure distribution reveals that no unphysical oscillations are produced by the KNPCT scheme whereas such spurious oscillations occur in the FD result without artificial viscosity. The errors computed relative to the $N = 144$ KNPCT solution are listed in Table 5. The measured rate of convergence for the KNPCT scheme of EOC $= 1.47$ is superior.

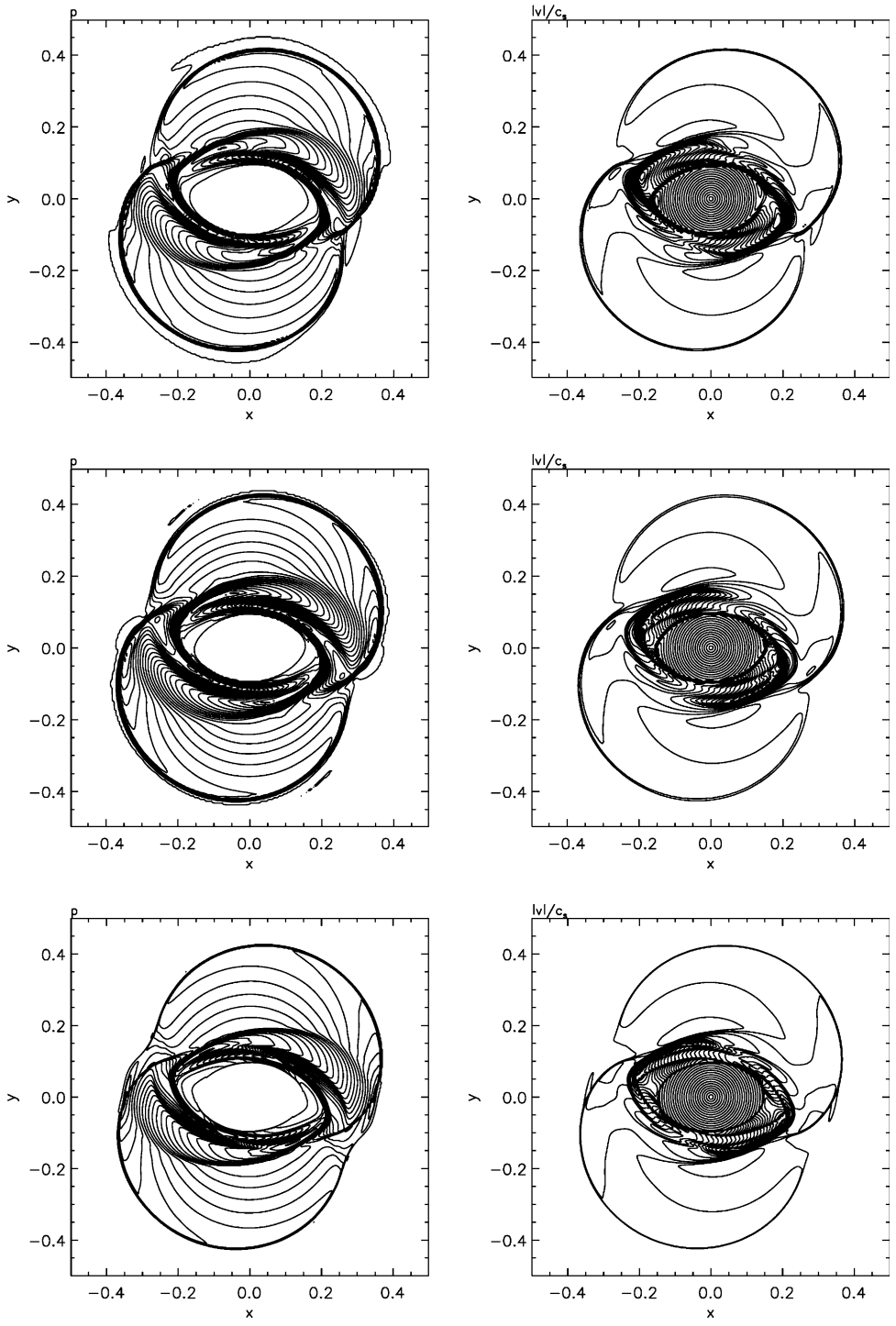

Fig. 7. Pressure contours (left panels) and contours of the Mach number (right panels) in the rotor problem for the FD solver (top) and KNPCT solver (middle) with $N = 400$, and for the reference solution (bottom). The pressure contours range from 0.0202 to 2.008 and the Mach number contours from 0 to 8.18.

Table 4
Rotor problem

N	FD			KNPCT		
	$\overline{E}$	EOC	Time (s)	$\overline{E}$	EOC	Time (s)
50	0.1773		5	0.1657		7
		0.84			0.85	
100	0.0991		37	0.0921		53
		0.76			0.97	
200	0.0587		345	0.0470		519
		0.63			1.29	
400	0.0378		2998	0.0190		4478

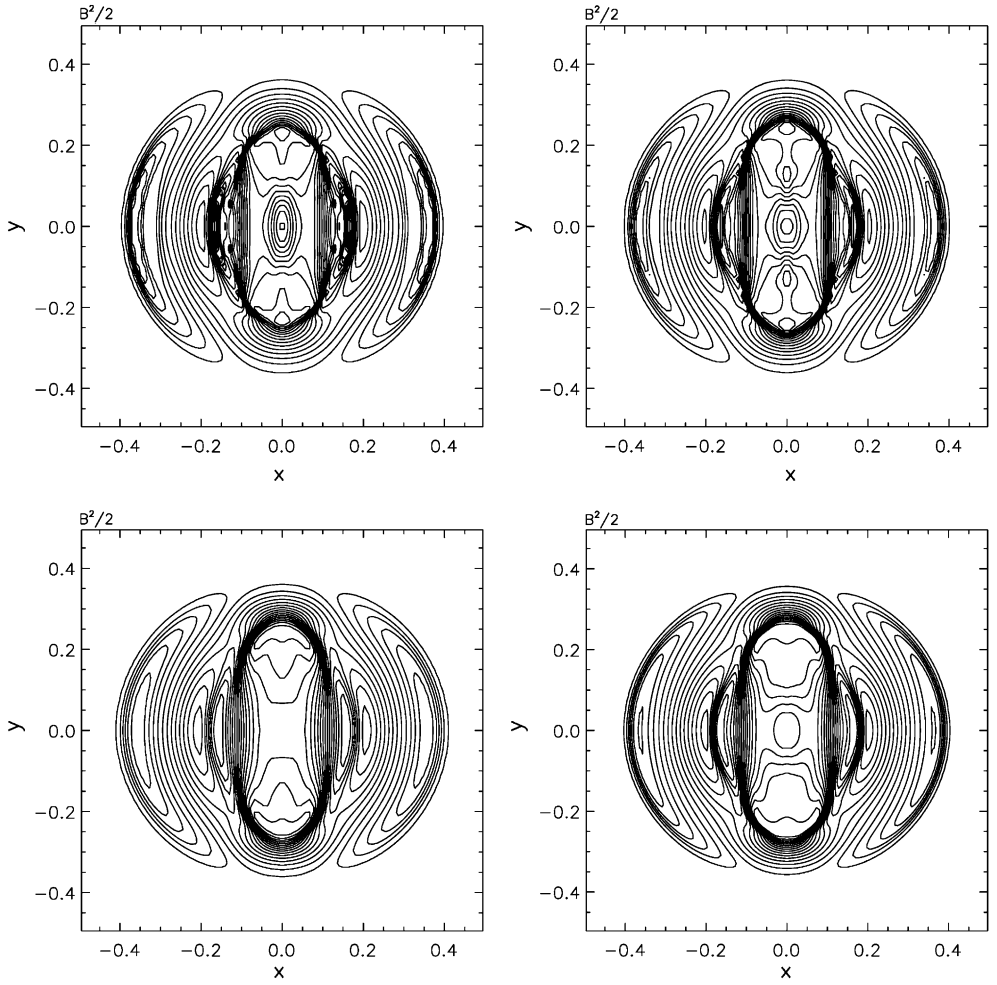

Fig. 8. Magnetic pressure $B^2/2$ in the spherical explosion problem for different runs: FD solver, $q = 0$, $N = 96$ (top left); FD solver, $q = 1.5$, $N = 96$ (top right); KNPCT solver, $N = 96$ (bottom left); reference solution (bottom right). The contour lines range from 2817 to 5932 corresponding to the minimum and maximum value obtained with the reference solution.

4.7. 3D: Shock–cloud interaction

As a further problem of astrophysical relevance I consider the interaction of a strong shock wave with a density clump in a magnetic environment. The initial conditions are taken from [39] (see also [10]), however,

Table 5
Spherical explosion

N	FD				KNPCT		
	$\overline{E}$[a]	$\overline{E}$	EOC	Time (s)	$\overline{E}$	EOC	Time (s)
64	0.1997	0.1613	0.67	1197	0.1635	1.47	1284
96	0.1813	0.1231	0.36	6581	0.0900		6882
144	0.1710	0.1062		39,386	0		37,948

[a] Without artificial viscosity.

extended to three space dimensions. Unfortunately, no literature solution is known to me (and likely there is none in 3D) which could be employed here as a means of comparison. Similar problems without magnetic field has been considered by the authors in [13,17,28]. The computational domain is a Cartesian box given by $(x,y,z) \in [-1/2,1/2]^3$. There is a discontinuity at $x = 0.1$ with left and right states:

$$\begin{pmatrix} \varrho \\ p \\ v_x \\ v_y \\ v_z \\ B_x \\ B_y \\ B_z \end{pmatrix}^L = \begin{pmatrix} 3.86859 \\ 167.345 \\ 0 \\ 0 \\ 0 \\ 0 \\ 2.1826182 \\ -2.1826182 \end{pmatrix}, \quad \begin{pmatrix} \varrho \\ p \\ v_x \\ v_y \\ v_z \\ B_x \\ B_y \\ B_z \end{pmatrix}^R = \begin{pmatrix} 1 \\ 1 \\ -11.2536 \\ 0 \\ 0 \\ 0 \\ 0.56418958 \\ 0.56418958 \end{pmatrix}.$$

Note that the discontinuity moves in $+x$ direction opposite to the highly supersonic flow right to the discontinuity. At $\mathbf{x} = (0.3,0,0)$ a spherical density clump with radius 0.15 is embedded having a constant density of 10. The clump is in pressure equilibrium with its surrounding medium. The adiabatic index $\gamma = 5/3$. Zero-gradient boundary conditions are used for all variables in all directions except at the upper x-boundary. There, variables except B_x are kept at their initial values. For B_x ghost zone values are calculated using the constraint $(\nabla \cdot \overline{\mathbf{B}})_{ijk} = 0$ directly to preserve solenoidality of the magnetic field at that boundary. Fig. 9 illustrates the geometrical setup of the problem.

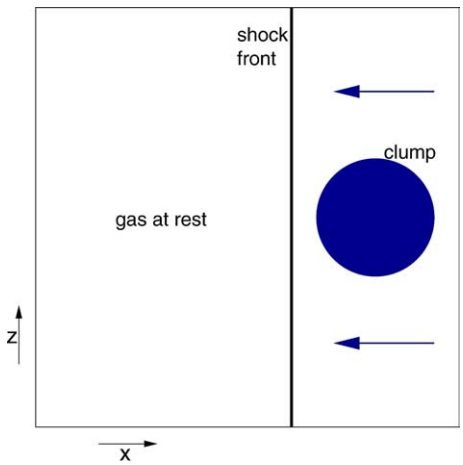

Fig. 9. Illustration of the setup of the shock–cloud interaction problem.

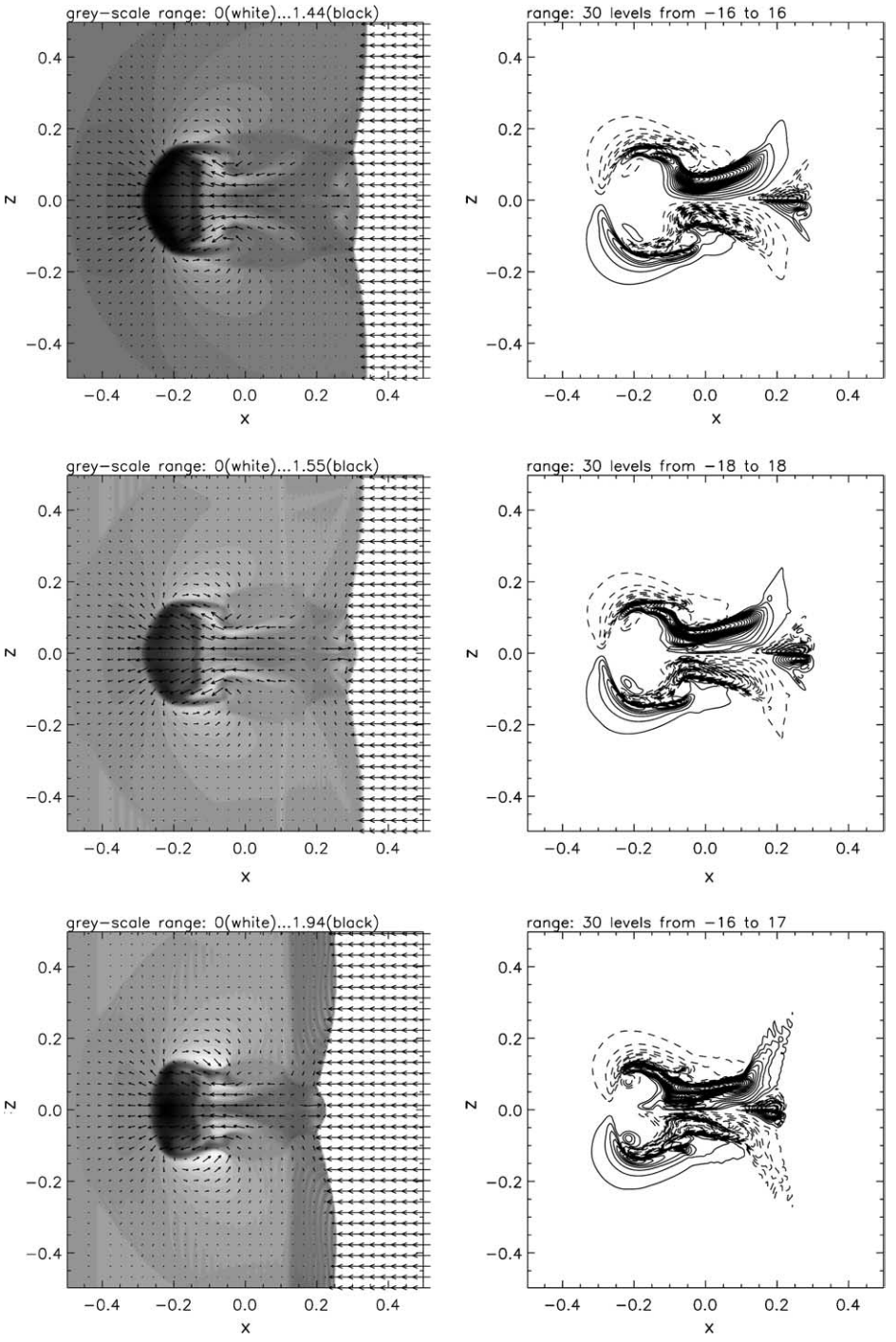

Fig. 10. Grey-scale representation of $\log \varrho$ with overlaid velocity field (left panels) and contour lines of B_x (right panels, solid lines correspond to positive values and dashed lines to negative values) in the x–z coordinate plane. $N = 200$ results for the KNPCT solver (top), FD solver with $q = 1.5$ (middle) and FD solver without artificial viscosity (bottom). Note the individual data range given in each plot.

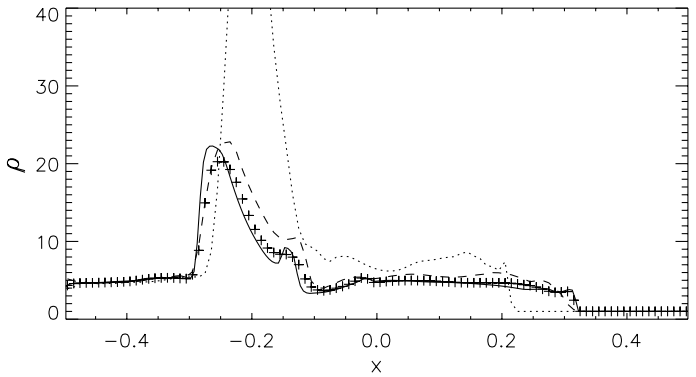

Fig. 11. Density profile along the x-axis for KNPCT (plus signs), FD with $q = 1.5$ (dashed line) and FD without artificial viscosity (dotted line) for a resolution $N = 100$. The solid line represents the reference solution.

Table 6
Shock–cloud interaction

N	FD				KNPCT		
	$\overline{E}$[a]	$\overline{E}$	EOC	Time (s)	$\overline{E}$	EOC	Time (s)
50	0.4029	0.1845	0.49	528	0.1515	1.00	167
100	0.3829	0.1313	0.07	8868	0.0757		4558
200	0.3786	0.1247		141,355	0		116,543

[a] Without artificial viscosity.

The simulations are carried out on a $N \times N \times N$ grid with varying number of zones $N = 50, 100, 200$. The KNPCT run with $N = 200$ serves as reference solution against which errors are measured. The simulations are stopped at evolution time $t = 0.06$ after which a violent collision between the shock and clump has taken place. The resulting density distribution and velocity field in the x–z coordinate plane are shown for the $N = 200$ runs in Fig. 10. Fig. 10 also demonstrates the generation of B_x during the collision. The FD result with artificial viscosity and the KNPCT result look similar although there are some significant differences between them. First, the shape and position of the discontinuity after the collision is not identical. Second, the resulting peak value in the density measured in the head of the clump is $\approx 20\%$ higher for FD. The neglect of artificial viscosity in the FD scheme leads to a rather distinct and obviously wrong picture: the discontinuity propagates too slow and the peak density reaches an unphysical high value of $\varrho_{\max} \approx 87$ to be compared with $\varrho_{\max} \approx 28$ for KNPCT. The discrepancies in the density structure are more clearly seen in Fig. 11 which shows a cut along the x-axis. Note also the existence of asymmetries and ripples in the tail of the B_x-profile not present in the KNPCT solution. The resulting averaged error, $\overline{E}$, and convergence rates are listed in Table 6. Note the extremely poor quality of the FD results obtained without artificial viscosity.

5. Concluding remark

The MHD solver presented in this paper is striking by its relative simplicity, robustness and efficiency. The main philosophy be at the bottom of it is a hybrid ansatz: the central-upwind scheme of Kurganov et al. [24] updates hydrodynamics including the Lorentz force term whereas Faraday's law is integrated using transport constraint techniques which preserve the divergence-free condition $\nabla \cdot \mathbf{B} = 0$ in discretized

form. As demonstrated by distinct test problems results are quite competing with those obtained by more sophisticated but also more intricate upwind schemes which must take into account the detailed eigenstructure of the system. A potential weakness of the proposed MHD scheme are the necessary averaging procedures to compute the upwind electric field flux. This step likely introduces additional numerical viscosity and effectively enlarges the numerical stencil. The latter means that an extension of the scheme to third-order accuracy, its application to adaptive grids and its transfer to massively parallel computers becomes more difficult.

References

[1] P. Arminjon, M.-C. Viallon, Généralisation du Schéma de Nessyahu–Tadmor pour Une Équation Hyperbolique á Deux Dimension D'espace, C. R. Acad. Sci. Paris 320 (série I) (1995) 85.
[2] F. Bianco, G. Puppo, G. Russo, SIAM J. Sci. Comput. 21 (1999) 294.
[3] J.U. Brackbill, Space Sci. Rev. 42 (1985) 153.
[4] J.U. Brackbill, D.C. Barnes, J. Comput. Phys. 35 (1980) 426.
[5] D.S. Balsara, D.S. Spicer, J. Comput. Phys. 149 (1999) 270.
[6] M. Brio, C.C. Wu, J. Comput. Phys. 75 (1988) 400.
[7] P. Colella, P.R. Woodward, J. Comput. Phys. 54 (1984) 174.
[8] A. Dedner, F. Kemm, D. Kröner, C.-D. Munz, T. Schnitzer, M. Wesenberg, J. Comput. Phys. 175 (2002) 645.
[9] P.J. Dellar, J. Comput. Phys. 172 (2001) 392.
[10] W. Dai, P.R. Woodward, J. Comput. Phys. 111 (1994) 354.
[11] W. Dai, P.R. Woodward, J. Comput. Phys. 142 (1998) 331.
[12] L.D. Zanna, N. Bucciantini, P. Londrillo, Astron. Astrophys. 400 (2003) 397.
[13] W.S. Don, C.B. Quillen, J. Comput. Phys. 122 (1995) 244.
[14] C.R. Evans, J.F. Hawley, Astrophys. J. 332 (1988) 659.
[15] S.K. Godunov, Mat. Sb. 47 (1959) 271.
[16] A. Harten, B. Engquist, S. Osher, S. Chakravarthy, J. Comput. Phys. 71 (1987) 231.
[17] H. Holden, K.-A. Lie, N.H. Risebro, J. Comput. Phys. 150 (1999) 76.
[18] P. Janhunen, J. Comput. Phys. 160 (2000) 649.
[19] G.-S. Jiang, E. Tadmor, SIAM J. Sci. Comput. 19 (1998) 1892.
[20] G.-S. Jiang, C.-W. Shu, J. Comput. Phys. 126 (1996) 202.
[21] A. Kurganov, D. Levy, SIAM J. Sci. Comput. 22 (2000) 1461.
[22] A. Kurganov, E. Tadmor, J. Comput. Phys. 160 (2000) 241.
[23] A. Kurganov, G. Petrova, Numer. Math. 88 (2001) 683.
[24] A. Kurganov, S. Noelle, G. Petrova, SIAM J. Sci. Comput. 23 (2001) 707.
[25] D. Levy, G. Puppo, G. Russo, SIAM J. Sci. Comput. 22 (2000) 656.
[26] D. Levy, G. Puppo, G. Russo, SIAM J. Sci. Comput. 24 (2002) 480.
[27] X.-D. Liu, S. Osher, T. Chan, J. Comput. Phys. 115 (1994) 200.
[28] J.O. Langseth, R.J. LeVeque, J. Comput. Phys. 165 (2000) 126.
[29] P. Londrillo, L. Del Zanna, Astrophys. J. 530 (2000) 508.
[30] P.D. Lax, Commun. Pure Appl. Math. 7 (1954) 159.
[31] X.-D. Liu, E. Tadmor, Numer. Math. 79 (1998) 397.
[32] H. Nessyahu, E. Tadmor, J. Comput. Phys. 87 (1990) 408.
[33] K.G. Powell, P.L. Roe, T.J. Linde, T.I. Gombosi, D.L. De Zeeuw, J. Comput. Phys. 154 (1999) 284.
[34] D. Ryu, T.W. Jones, A. Frank, Astrophys. J. 452 (1995) 785.
[35] D. Ryu, F. Miniati, T.W. Jones, A. Frank, Astrophys. J. 509 (1998) 244.
[36] C.-W. Shu, S. Osher, J. Comput. Phys. 77 (1988) 439.
[37] C.-W. Shu, S. Osher, J. Comput. Phys. 83 (1989) 32.
[38] J.M. Stone, M.L. Norman, Astrophys. J. Suppl. Ser. 80 (1992) 791.
[39] G. Tóth, J. Comput. Phys. 161 (2000) 605.
[40] W.-M. Tscharnuter, K.-H. Winkler, Comput. Phys. Commun. 18 (1979) 171.
[41] B. van Leer, J. Comput. Phys. 23 (1977) 276.
[42] A.L. Zachary, A. Malagoli, P. Colella, SIAM J. Sci. Comput. 15 (1994) 263.
[43] U. Ziegler, Astron. Astrophys. 313 (1996) 448.

[44] U. Ziegler, P. Ulmschneider, Astron. Astrophys. 327 (1997) 854.
[45] U. Ziegler, Comput. Phys. Commun. 109 (1998) 111.
[46] U. Ziegler, Comput. Phys. Commun. 116 (1999) 65.
[47] U. Ziegler, G. Rüdiger, Astron. Astrophys. 401 (2003) 433.